Document downloaded from:

http://hdl.handle.net/10251/170079

This paper must be cited as:

Inhestern, LB.; Braun, J.; Paniagua, G.; Serrano, J. (2020). Design, Optimization, and Analysis of Supersonic Radial Turbines. Journal of Engineering for Gas Turbines and Power. 142(3):1-12. https://doi.org/10.1115/1.4044972

The final publication is available at

https://doi.org/10.1115/1.4044972

Copyright ASME International

Additional Information

Proceedings of the ASME 2019 Turbomachinery Technical Conference & Exposition
ASME 2019 Turbo Expo
June 17-June 21, 2019, Phoenix AZ, USA

GT2019-91756

DRAFT: DESIGN, OPTIMIZATION AND ANALYSIS OF SUPERSONIC RADIAL TURBINES

Lukas Benjamin Inhestern

CMT-Motores Térmicos
Universitat Politècnica de València
Valencia 46022, Spain.
Email: luin@mot.upv.es

James Braun

Zucrow Laboratories
Purdue University
West Lafayette, IN 47906, USA.
Email: braun26@purdue.edu

Guillermo Paniagua

Zucrow Laboratories
Purdue University
West Lafayette, IN 47906, USA.
Email: gpaniagua@purdue.edu

José Ramón Serrano

CMT-Motores Térmicos
Universitat Politècnica de València
Valencia 46022, Spain.
Email: jrserran@mot.upv.es

ABSTRACT

New compact engine architectures such as pressure gain combustion require ad-hoc turbomachinery to ensure an adequate range of operation with high performance. A critical factor for supersonic turbines is to ensure the starting of the flow passages, which limits the flow turning and airfoil thickness. Radial outflow turbines inherently increase the cross section along the flow path, which holds great potential for high turning of supersonic flow with a low stage number and guarantees a compact design. First the preliminary design space is described. Afterwards a differential evolution multi-objective optimization with 12 geometrical design parameters is deducted. With the design tool AutoBlade 10.1, 768 geometries were generated and hub, shroud, and blade camber line were designed by means of Bezier curves. Outlet radius, passage height, and axial location of the outlet were design variables as well. Structured meshes with around 3.7 million cells per passage were generated. Steady three dimensional Reynolds averaged Navier Stokes (RANS) simulations, enclosed by the k-omega SST turbulence model were solved by the commercial solver CFD++. The geometry was optimized towards low entropy and high power output. To prove the functionality of the new turbine concept and optimization, a full wheel unsteady RANS simulation of the optimized geometry exposed to a nozzled rotating detonation combustor (RDC) has been performed and the advantageous flow patterns of the optimization are recognized.

NOMENCLATURE

Latin Letters

A Area
CFD Computational Fluid Dynamics
c Absolute velocity
c_p Isobaric heat capacity
LE Leading edge
M Mach number
$\dot{m}$ Massflow
PS Pressure side
P Pressure
PDC Pulse Detonation Combustor

R Radius
RDC Rotating Detonation Combustor
RRDE Radial Rotating Detonation Engine
SS Suction side
T Temperature
TE Trailing edge
v Relative velocity
$\dot{W}$ Power
w Specific power
y^+ Nondimensional wall distance
Z Axial coordinate

Subscripts

in Inlet
$surf.$ Surface
tot Total or stagnation conditions
tt Total-to-total
u Circumferential component

Greek Letters

α Absolute flow angle
β Relative flow angle
γ Isentropic exponent
ε Tip gap height
κ Channel turning angle
θ Circumferential coordinate
ω Rad speed
τ Torque
η efficiency

Symbols

$\overline{\ }$ Averaged value

INTRODUCTION

In traditional engines that follow the Joule/Brayton cycle, conventional deflagration combustors deliver low Mach numbers at the inlet of the turbine, with typical values around Mach 0.1 [1]. At such low subsonic inlet speeds, high turning angles can be achieved throughout the turbine nozzle guide vane, while guaranteeing that the flow remains unchoked by satisfying the isentropic limit. Similar to the design of subsonic stators, supersonic passages should comply with isentropic limit, and hence constrains the maximum turning angle. In contrast to the subsonic case, higher supersonic inlet Mach numbers allow for higher turning in the supersonic vane [2]. Higher Mach numbers however are accompanied by higher pressure loss, consequently the designer should compare power output versus pressure loss. To increase the cycle efficiency, new cycles such as detonation (pressure gain) cycles can achieve higher stagnation pressure due to a near constant combustion [3]. This near constant volume combustion is accompanied by a higher cycle efficiency. For the same turbine inlet conditions, the detonation-based cycle results in a significant lower production of entropy, hence delivering a higher cycle efficiency. Several detonation engine architectures exist. A first one is a pulse detonation combustors (PDC) in which a cyclic refill occurs in a tube [4]. Another architecture is a rotating detonation combustor (RDC) in which a rotating shock continuously burns the fuel. In RDCs, Mach number at the outlet of the combustor is around one with fluctuations below and above the speed of sound [5]. These type of combustors have been experimentally investigated since the 60s [6, 7, 8] and numerically [9, 10]. Finally, reduced models to get fast predictions of the flow field have been presented via method of characteristics solvers [2, 11].

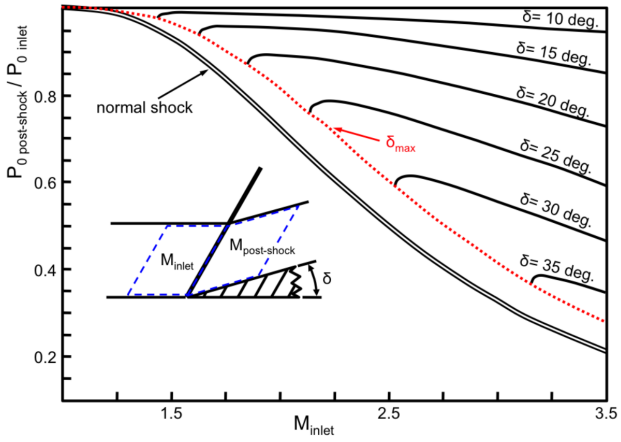

FIGURE 1: TOTAL PRESSURE ACROSS A NORMAL SHOCK AND OBLIQUE SHOCKS

Paniagua et al. [12] found that there will be a loss of 80 percent when diffusing from Mach 3.5 to subsonic (Fig. 1). Hence, to efficiently cope with these high Mach number flow and pressure fluctuations, new turbine classes need to be designed and several architectures for efficient downstream power extraction are possible. A first choice is to integrate the turbine with a diffuser to reduce significantly the turbine entry Mach number, which then would allow to use conventional axial turbines, however this requires a rather long diffuser, or an integration of the diffuser with the turbine nozzle guide vane [13]. The optimization of the nozzle guide vane end walls can result in an efficiency of about 80%. The increase of efficiency compared to a baseline turbine without contouring was above 30 percentage points. Another solution is to design nozzles to further boost the Mach number, damp the flow angle fluctuations and design axial supersonic turbines. This class of turbine was developed by Paniagua et al. [14] and Sousa et al. [2] and is characterized by axial supersonic flow throughout the passage, slender airfoils with limited turning to remain below the Kantrowitz limit [15] and guarantee starting of the turbine. Recently Sousa et al. [16] performed an engine analysis with a reduced model of the rotating detonation

combustor and the supersonic turbine. They found an increase of several percentage points at lower compression ratios for a turbo jet engine configuration. Finally, Huff et al. [17] experimentally investigated radial inflow turbines coupled to a radial rotating detonation engine (RRDE) enabling a compact design with power output of 70 kW. Higashi et al. [18] also tested a centrifugal compressor, RDC and single stage radial flow turbine. Akbari and Polanka test pressure gain combustor devices with radial turbine designs as well [19].

This paper describes the design procedure for compact radial outflow turbines for supersonic flows. First, the design method and space is described followed by an optimization and finally a full unsteady investigation of rotating detonation waves exposed to optimized radial outflow turbines.

DESIGN & OPTIMIZATION

Baseline design

For the successful design of supersonic turbines the Kantrowitz line plays an important role. The area ratio of the throat A_{throat} to inlet area A_{inlet} needs to be above the Kantrowitz line to allow a self starting of the turbine and thus, entering of the supersonic flow as it is shown in Fig. 2.

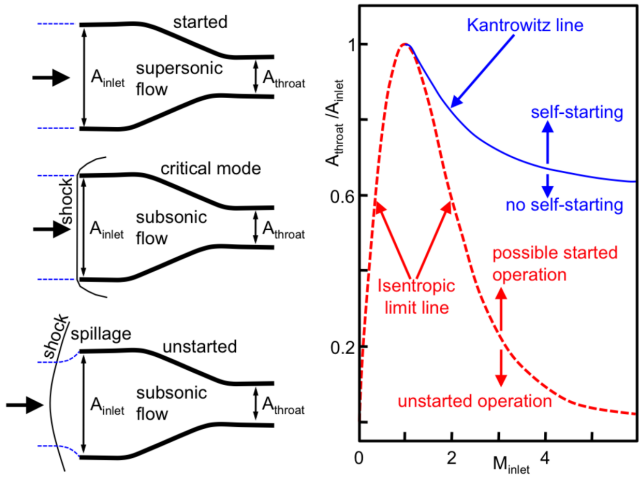

FIGURE 2: KANTROWITZ CONDITION FOR STARTING OF SUPERSONIC INFLOW

In conventional supersonic turbines the criteria of a large enough A_{throat} restricts the turning of the flow and thus, the wheel torque. Hence radial outflow designs with inherently increasing cross section are favorable to obtain high flow turning and compact machine designs. To be able to combine an axial outflow RDC with the designed turbine an axial inflow into the turbine passage must be realized. Figure 3 shows the chosen passage geometry for the baseline design of the novel axial inflow radial outflow turbine. A circular shroud curvature, as can be found in the radial outflow compressor design by McKain and Holbrook [20], and a constant passage height was defined. The passage shroud turning radius to passage height ratio (1.5) has the order of commonly found radial turbomachinery. The passage height was kept constant to guarantee a expansion of the flow cross section as shown in Fig. 4. From these design constraints an outlet diameter of 0.22 m was retrieved. Hence, the ratio of orthogonal

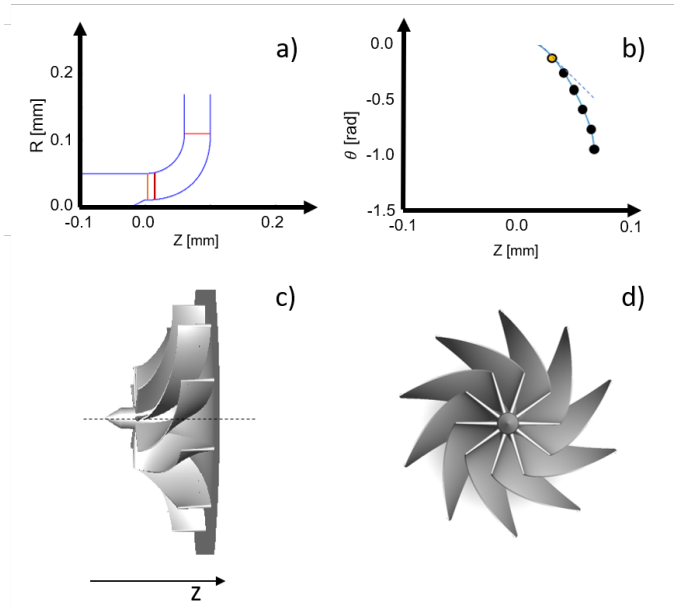

FIGURE 3: BASELINE GEOMETRY WITH: a) PASSAGE, b) CAMBERLINE, c) SIDE VIEW OF 3D ROTOR GEOMETRY, d) TOP VIEW OF 3D ROTOR GEOMETRY

passage area to inlet duct area is monotonously increasing, so that the smallest area A_{throat} can be found at the inlet of the turbine passage giving freedom to high flow turning. However, considering the thickness of the blades at the leading edge, the cross section area at the inlet can significantly be reduced and endanger the self-starting of the passage. Thus, the leading edge had to be cut back towards higher axial positions, where $A_{\text{throat}}/A_{\text{inlet}}$ has a higher value, until the passage was started.

The blades are designed with a blade thickness of 1.6 mm at the hub and of 0.8 mm at the tip. A tip gap of 0.4 mm height was assumed. The camberline was designed by means of a Bezier curve defined by six control points constantly distributed over the blade as shown in Fig. 3 b). The same distribution of rel. chord length to θ was defined at hub and shroud. The first point was set to obtain zero incidence at the inlet. The design speed at the

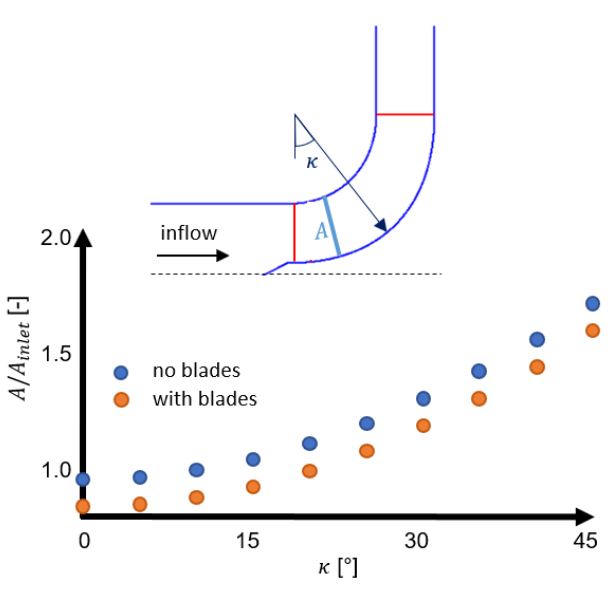

FIGURE 4: AREA RATIO WITH AND WITHOUT BLADES

outlet tip was set to 650 m s^{-1}. McKain and Holbrook [20] state stress stability for even higher centrifugal forces acting on blades with comparable blade thickness. The resulting wheel geometry was modeled with BladeGen (NUMECA) and is shown in Fig. 3 c). A relatively low blade number of 10 was chosen to reduce the number of leading edge shocks entering the passage and increase the self starting probability. The inlet bulb was designed as a cone to reduce shock losses in the inlet.

During a preliminary design phase, numerous geometries were evaluated to maximize the outlet blade angle. An increase in the b-angle at low chord length prevents flow separation at the shroud due to the guidance from axial to radial flow direction. However, a large increase causes flow separation on the pressure side close to the leading edge on the blade, which restricts the design space. Although a higher outlet blade turning reduces the passage cross section, reducing the exit flow velocity, a maximum flow turning was identified to be most beneficial for torque production. The maximum outlet bade angle was restricted by flow separations close to the outlet, where centrifugal forces and blade angle are high. Thus, an outlet blade angle at the shroud of 42 deg. and at the hub of only 14 deg. was realized. While the restraint on the outflow angle limits the power extraction, high shock losses in the inflow section and at the leading edge potentially reduces efficiency of the expansion device.

CFD Setup

For the computational domain of the optimization a 80 mm long inlet duct was modeled upstream of the tip of the inlet bulb. As shown in Fig. 5 the outlet of the domain was set 60 mm behind the trailing edge of the blade. To reduce the numerical ex-

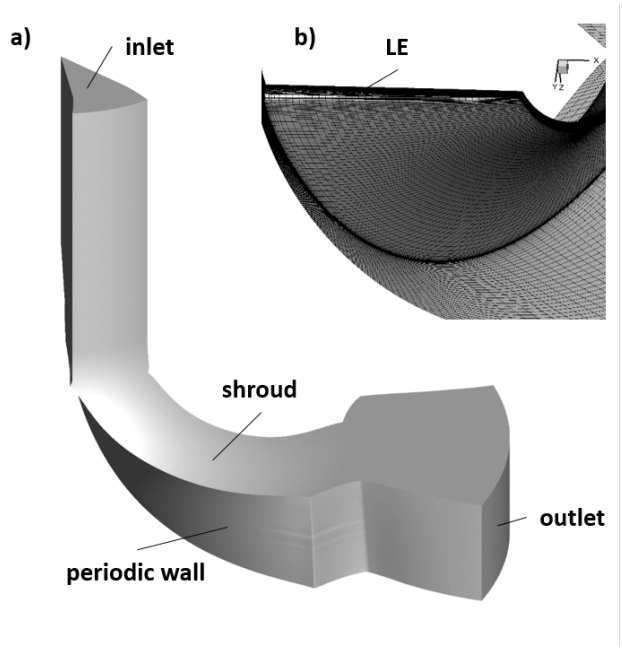

FIGURE 5: a) COMPUTATIONAL DOMAIN, b) FINAL MESH SETUP

penses of the optimization, steady 3D Reynolds averaged Navier Stokes (RANS) simulations, enclosed by the k-omega SST turbulence model, were solved for only one blade passage by the commercial solver CFD++ [21]. The solver was validated with a Mach 5 ramp case to demonstrate the shock boundary layer interaction was fully resolved [22]. The solver was further validated with experimental results of a transonic vane with supersonic outlet flow [23]. In the contourplot of the Mach number at midspan (Fig. 6 a), the trailing edge shock impinging on the neighboring vane suction side is visualized. The comparison of the CFD and experiments for the isentropic Mach number on the vane (Fig. 6 b)) shows good agreement and the error at the location of the shock impingement is around 0.3%.

While the inlet boundary conditions were set by imposing the M_{in}, T_{in}, and p_{in} according to the values in Tab. 1, the outlet boundary was set to the supersonic outlet condition. By means of NUMECAs AutoGrid5 three different structured grids with a HOH block structure were generated to demonstrate mesh convergence of the two optimization objectives (shaft power and mass flow averaged entropy 30 mm behind the trailing edge). As can be seen in Tab. 2 the relative derivation from the finest mesh results is small. Due to the small difference (below 0.25 percent) between "medium" and "fine" the mesh, the middle cell density was considered for this study. However, since the geometry

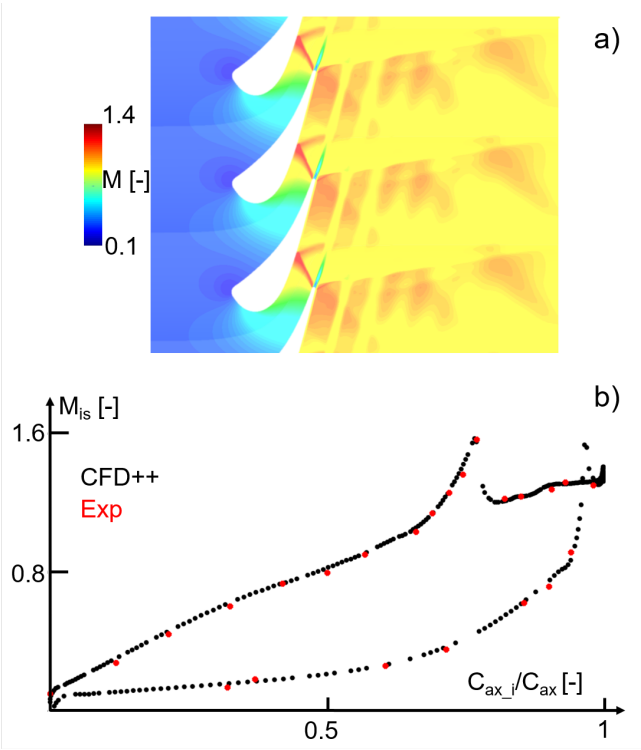

FIGURE 6: TRANSONIC VANE AT MID-SPAN: a) MACH CONTOUR AND STREAMWISE VARIATION OF b) ISENTROPIC MACH NUMBER

M_{in}	2
T_{in}	1380 K
P_{in}	0.5000 bar
$T_{t,in}$	2283 K
$P_{t,in}$	4.386 bar
$\dot{m}$ (one passage)	0.1481 kg s^{-1}
$\dot{m}_{red.}$ (one passage)	1.614 kg s^{-1} bar^{-1} K$^{0.5}$

TABLE 1: INLET BOUNDARY CONDITION

changes and might increase its passage length, more cells are required for the optimization. Additionally, a strict compliance a y^+-value below one is desired. Thus, the final mesh with around 3.79 million cells per passage and a maximum y^+-value of 0.84 was selected. The tip gap was meshed with 41 cells between upper blade surface and shroud.

	Coarse	Medium	Fine
$\left(\frac{s_{out}-s_{out,Fine}}{s_{out,Fine}}\right)$	0.0359 %	0.0077 %	0.0000 %
$\left(\frac{\dot{W}-\dot{W}_{Fine}}{\dot{W}_{Fine}}\right)$	-0.296 %	0.032 %	0.000 %
$\left(\frac{\eta_{tt}-\eta_{tt,Fine}}{\eta_{tt,Fine}}\right)$	-1.75 %	-0.22 %	0.00 %
max. y^+	4.45	2.23	0.84
Cells	1933824	2972224	3792960

TABLE 2: MESH CONVERGENCE ANALYSIS

Parametrization

For the multi-objective optimization of the turbine wheel, twelve design points were selected as ideal amount of parameters as more points did not significantly affect the design space and fewer points would reduce the design space. Therefore, hub and shroud were replaced by Bezier curves, which are each defined by two control points (CPs) (one at the inlet and one at the outlet) as shown in Fig. 7. Bezier curves were used to guarantee continuity in the curvature and allows for a high amount of variation by changing the control points. While inlet CPs had only the freedom to move in the axial direction, the outlet CPs had only freedom to shift in the radial direction. To guarantee monotonous

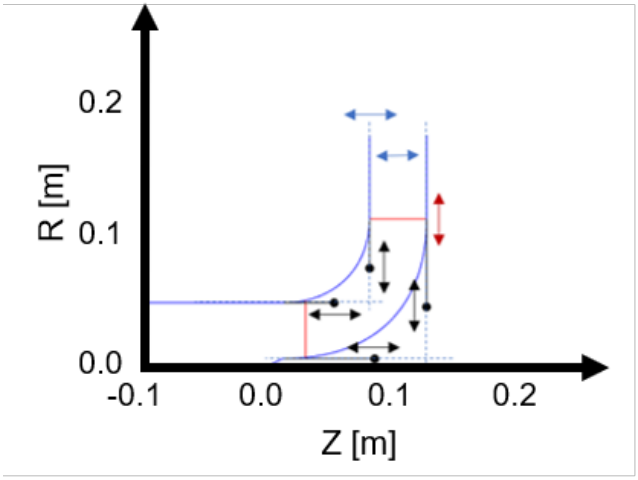

FIGURE 7: HUB AND SHROUD PARAMETRIZATION VIA BEZIER CURVES

curvatures of hub and shroud, the variability of inlet CPs was limited by the outlet wall Z-coordinate and the variability of the outlet CPs was limited by the inlet wall R-coordinate as visible in Fig. 7. Furthermore, freedom was given to the Z-coordinate

of the shroud at the passage outlet and to the passage height. Since flow towards higher radii results into a reduction of the power w according to Eqn. 1 but at the same time allow a further acceleration and higher flow turning, the blade outlet radius was set as optimization parameter as well.

$$w = \frac{c_1^2 - c_2^2}{2} + \frac{v_2^2 - v_1^2}{2} + \frac{\omega^2}{2}\left(\frac{r_1^2}{r_2^2} - 1\right) \tag{1}$$

Similarly, it was decided that the outlet tip velocity remained constant. This way only the aerodynamic part $c_{u,2}$ of the Euler's turbomachinery equation with no swirled inflow (Eqn. 2) was evaluated in the optimization.

$$w = -c_{u,2}u_2 \tag{2}$$

Furthermore, the first control point of the Bezier curve of the camberline was adjusted according to the set rpm to obtain zero incidence at the tip of the blade. All other control points of the camberline were set as free optimization parameters. An important parameter to secure a high number of started turbine passages ("individuals") was the definition of the Z-coordinate of the leading edge. For this parameter the location was imposed to obtain the same area ratio $A_{\text{throat}}/A_{\text{inlet}}$ as in the baseline design depending on generated hub and shroud geometries.

Optimization Procedure

The genetic optimizer CADO [24, 25, 26, 27] was used in this work and is a differential evolution multi-objective optimization tool. The two selected optimization objectives were minimum mass flow averaged outflow entropy and maximum shaft power.

SUPERSONIC OPTIMIZATION RESULTS

The multi-objective optimization generated 31 populations which contained 768 converged geometries and formed a Pareto front according to the objective values power and outlet entropy as depicted Fig. 8. Along the Pareto front an increase in outlet entropy relates linearly with an augmentation of shaft power. At the Pareto front, higher power is accompanied by high turning angle and an increase in TE radius. These parameters extend the flow path and thus, increase the aerodynamic loss together with the outlet entropy. However, the increase of aerodynamic losses is relatively low compared to the power gain as can be observed by the plotted total-to-total isentropic efficiency according Eqn. 3. Towards the individual with highest power, the efficiency increases monotonously. Further it was observed that the outlet passage height is increased when the efficiency rises. The increase of the passage height causes additional cross section area

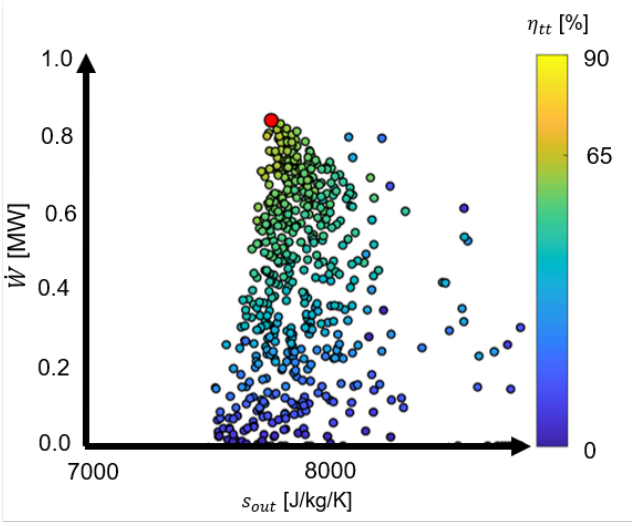

FIGURE 8: OPTIMIZATION RESULTS

at the outlet resulting in higher flow acceleration without noticeable extension of the flow path. Hence, power increases while aerodynamic losses are less influenced. This makes the outlet passage height an important design parameter for supersonic radial turbines as well as for axial turbines [28].

$$\eta_{\text{tt}} = \frac{\omega\tau}{\dot{m}T_{\text{tot,in}}\bar{c}_{\text{p}}\left[1 - \left(\frac{\bar{p}_{\text{tot,out}}}{\bar{p}_{\text{tot,in}}}\right)^{\left(\frac{\bar{\gamma}-1}{\bar{\gamma}}\right)}\right]} \tag{3}$$

Furthermore, it turns out that the power penalty due to a higher outlet radius demonstrated by Eqn. 1, controls the power gain which results from a larger wheel outlet area with consequent further flow acceleration and the benefit of a longer passage allowing smoother flow turning. Since the outlet tip speed was fixed for all geometries, centrifugal forces are reduced in the outlet region. Furthermore, longer blades and thus, smoother curvatures can be realized due to extended hub and shroud lines. This way a higher blade turning without flow separations in the outlet section seems feasible. The power penalty according to Eqn. 1 is subordinate. The optimal solution expands the working fluid over a total pressure ratio of 4.86 and a total temperature ratio of 1.243. It delivers 831 kW and thus, 728 kW more than the baseline design, and with 65.4 % nearly 45 % more efficiency. This is primarily achieved by ensuring the turbine passage is started, preventing both the appearance of a standing normal shock and the abatement of the separated region. In turbochargers, radial turbines exposed to transients into off-design operation exhibit reductions in efficiency of nearly 40% [29] (in stationary ICE condition). Conventional axial turbine exposed high inlet flows deliver an efficiency of barely 50%, however the optimization of

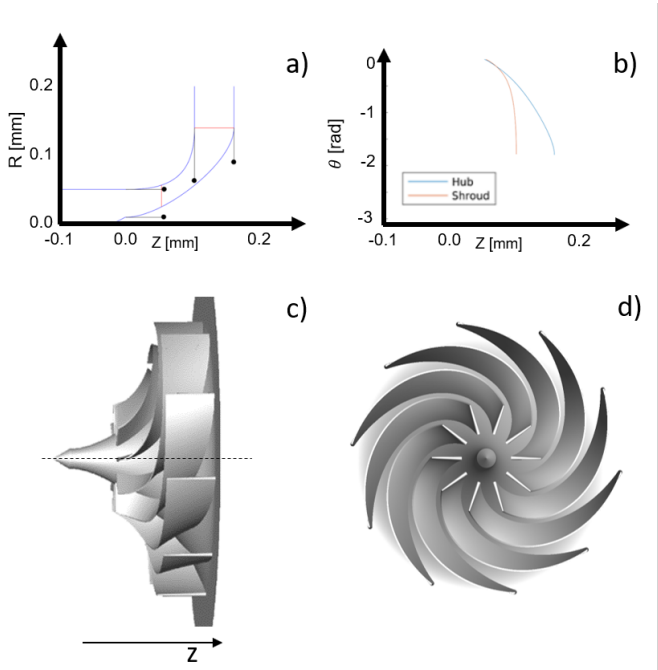

FIGURE 9: OPTIMIZED GEOMETRY WITH: a) PASSAGE, b) CAMBERLINE, c) SIDE VIEW OF 3D ROTOR GEOMETRY, d) TOP VIEW OF 3D ROTOR GEOMETRY

the endwall can yield over 30% of efficiency improvement [30].

Comparing the optimized passage in Fig. 9 a) with the baseline passage in Fig. 7 aforementioned conclusions can be confirmed. Table 3 summarizes the geometrical details of the optimized geometry compared to the baseline case. The optimized geometry has a higher outlet diameter of 295 mm combined with a higher passage height. Like in the baseline design, the highest change of the blade curvature appears at relatively low chord-length as shown in Fig. 9 b). The outlet blade turning was increased significantly to 72 deg at the shroud. Figure 9 d) shows that the blade normal distance to the neighbor blade remains rather constant, which decreases flow separation. Hence the outlet passage height is the main driver behind the increase in cross section area and hence flow acceleration. The outlet diameter in combination with the constant outlet speed gives the reduced blade tip speed of 937 rpm/K$^{0.5}$ for the optimized geometry.

For a given inlet diameter that depends on the upstream combustor and/or nozzle, the following design criteria can be drawn to achieve high efficient axial inflow radial outflow supersonic turbines:

1. Cutting back of leading edge to achieve self-starting ability.
2. Extending hub inlet bulb for advantageous shock system.
3. Aiming for continuously growing passage cross section and high blade turning.

	Baseline	Optimized
$D_{\text{shroud,in}}$	100 mm	100 mm
$D_{\text{hub,in}}$ $\left(\frac{D_{\text{hub,in}}}{D_{\text{shroud,in}}}\right)$	20 mm (0.2)	20 mm (0.2)
z_{LE} $\left(\frac{z_{\text{LE}}}{D_{\text{shroud,in}}}\right)$	15 mm (0.15)	53 mm (0.15)
h_{LE} $\left(\frac{h_{\text{LE}}}{D_{\text{shroud,in}}}\right)$	40 mm (0.4)	30 mm (0.3)
h_{TE} $\left(\frac{h_{\text{TE}}}{D_{\text{shroud,in}}}\right)$	40 mm (0.40)	59 mm (0.59)
ε_{LE} $\left(\frac{\varepsilon_{\text{LE}}}{h_{\text{LE}}}\right)$	0.4 mm (0.01)	0.4 mm (0.013)
ε_{LE} $\left(\frac{\varepsilon_{\text{TE}}}{h_{\text{TE}}}\right)$	0.4 mm (0.01)	0.4 mm (0.0068)
D_{out} $\left(\frac{D_{\text{out}}}{D_{\text{shroud,in}}}\right)$	220 mm (2.2)	295 mm (2.95)
$\beta_{\text{out,hub}}$	14 deg	55 deg
$\beta_{\text{out,shroud}}$	42 deg	72 deg

TABLE 3: GEOMETRY SPECIFICATION OF BASELINE AND OPTIMIZED GEOMETRY

4. Reaching high levels of blade turning at low chord length avoids separations at the shroud at the inlet of the turbine passage.
5. Increasing passage height for cross section expansion.
6. Keeping a rather constant blade normal distance which results from high blade turning.
7. Comparing geometries with constant outlet speed with higher outlet radius reduce centrifugal forces and thus flow separation in exducer. This allows higher turning angles. Furthermore, a higher outlet radius gives more area potential which can be invested in flow turning or flow acceleration.
8. Extending hub and shroud lines allow longer blades and thus, smother curvatures. Hence, flow separation and flow turning can be improved.

OPTIMIZED GEOMETRY AERODYNAMICS

As observed in Fig. 9 a) and in Fig. 9 c) the leading edge of the blade is relatively far downstream from the inlet bulb. The shock structure at the inlet of the turbine wheel in Fig. 10 shows that a far downstream position is profitable for the shock losses. Instead of entering the passage with a Mach number of 2, the Mach number is reduced due to the diagonal shocks of the inlet cone and due to compression waves of the hub. Additionally, the cone shock reflects at the shroud causing a local separation, which reattaches before entering the blade passage. As observed in Fig. 10, the supersonic flow penetrates the turbine passage, oblique shocks are formed at both endwalls, the supersonic diffuser is started as it complies with the isentropic limit in the Kantrowitz shown in Fig. 2.. Thus, the leading edge

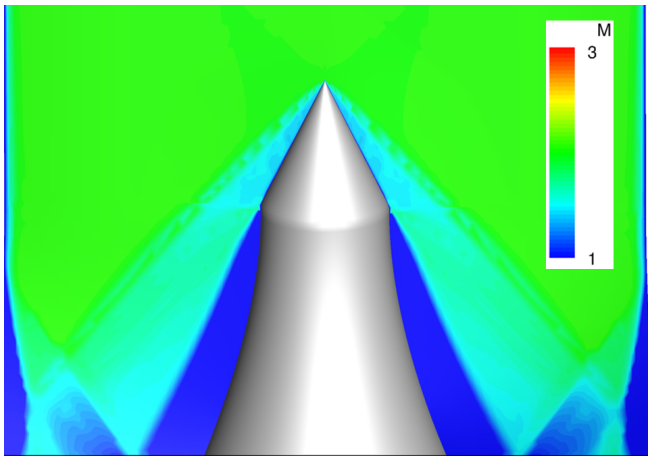

FIGURE 10: INFLOW SHOCK STRUCTURE

shock which appears to be relatively orthogonal due to the low Mach number for all simulated geometries has lower intensity. Although the absolute and relative Mach number is locally reduced below 1, the turbine is started as seen at 10 % span in Fig. 11(a). At higher radial positions like 50 % span in Fig. 11(b) and 75 % span in Fig. 11(c) the relative inlet Mach number is reduced to values of around 1.6 due to the shock structure at the inlet. The leading edge shock enters the passage diagonally. In Fig. 12 the static surface pressure is shown and the entering shocks that cause shock impingement are observed. These shock impingements are dominant on the pressure side and leads to further blade loading and power. The static pressure distribution at 75 % span shows that the leading edge shock first hits the suction side, which can be explained by the incoming flow angle. Afterwards, the shock is reflected and hits the pressure side of the next blade. Also, the shock that first arrives the pressure side is clearly reflected to the suction side. However, the reflection angle is much sharper due to the convex curvature of the pressure side.

Subsonic inflow

When the flow enters the blade passage, the flow experiences a reduction of the cross sectional area due to the thickness of the blades (Fig. 4). The optimized geometry and most generated radial turbine geometries have a monotonously growing passage cross section. While the curvature of the hub introduces compression waves, the convex shape of the shroud introduces expansion waves over a significantly larger circumference. Hence, the turbine passage owns characteristics, which are favorable to perform a transition of subsonic to supersonic flow. Thus, the starting of the passage when the inlet is subsonic, was assessed.

To ensure a fair comparison of the performance parameters, the inlet mass flow was maintained to the one of the supersonic

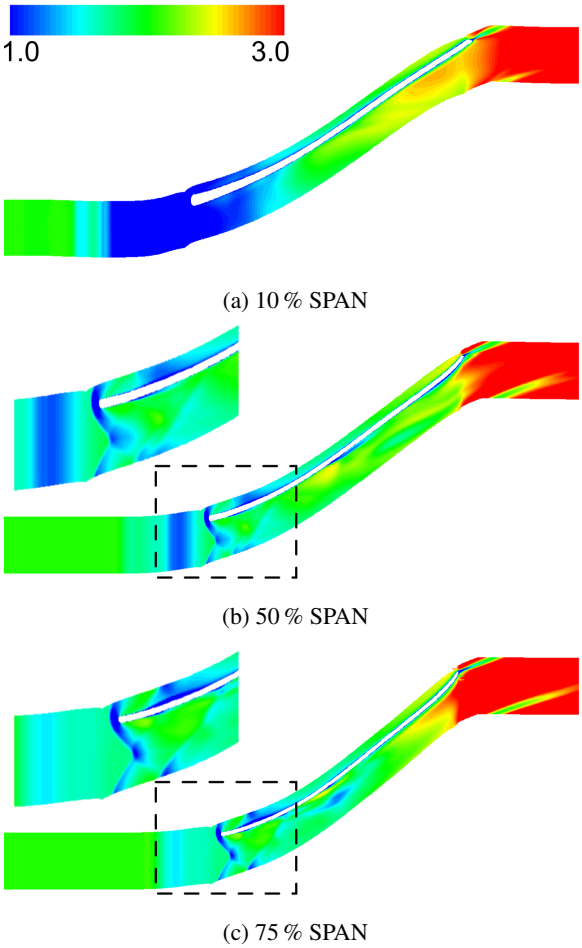

(a) 10 % SPAN

(b) 50 % SPAN

(c) 75 % SPAN

FIGURE 11: RELATIVE MACH NUMBER OF OPTIMIZED GEOMETRY WITH SUPERSONIC INFLOW

inlet condition. Furthermore, the total inlet temperature was kept constant to simulate the same reduced rotational speed. By setting these subsonic boundary conditions, an inlet Mach number of around 0.6 stabilized in the inlet duct. As can be seen in Fig. 13, the relative Mach number reaches one close the throat (LE) of the passage at all spans. From the LE the flow continuously accelerates, as depicted in Fig. 14. However, due to the concave surfaces of hub and blade pressure side, the flow takes longer for a complete transition to fully developed supersonic flow close to this surface. The flow is accelerated until it reaches high relative outlet Mach numbers of around 3 and absolute Mach numbers of around 2 in the stationary frame of reference.

Due to the subsonic inflow no leading edge shock develops, which significantly reduces the overall losses of the turbine. Also, further shock reflections and following loss generation mechanisms are diminished as visualized in Fig. 14 and in Fig. 15. Due to the subsonic inflow, the surface pressure level is high

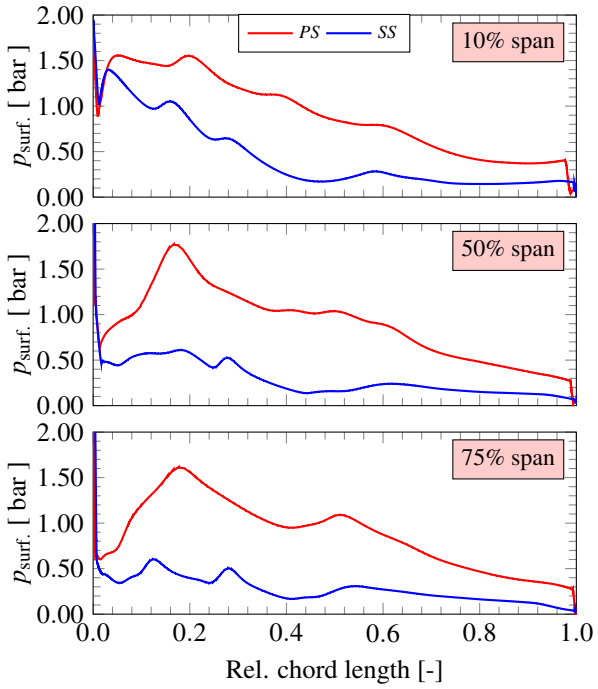

FIGURE 12: SURFACE PRESSURE PROFILES 10 %, 50 %, AND 75 % SPAN WITH SUPERSONIC INFLOW

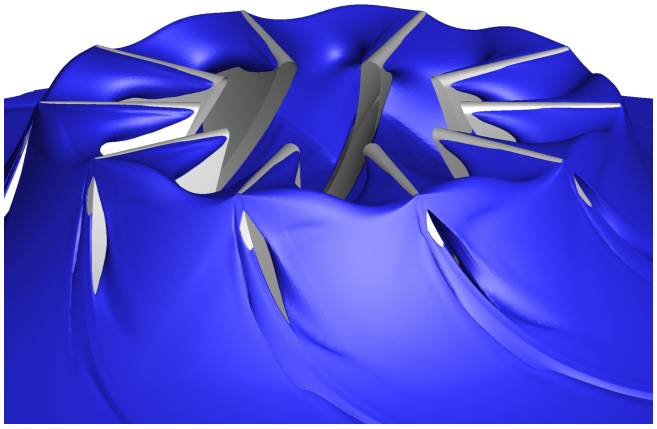

FIGURE 13: ISO-SURFACE AT MACH ONE WITH SUBSONIC INFLOW

near the the inlet section. The surface pressure distributions appears smoother and does not show shock impingement patterns. However, at 30 % chord length a local flow separation occurs on the suction side. In general, the flow quality was improved significantly by using subsonic instead of supersonic inflow. Although the turbine power is slightly reduced to 807 kW, the total-to-total efficiency increases considerably to 79.1 %. Lower losses reduce

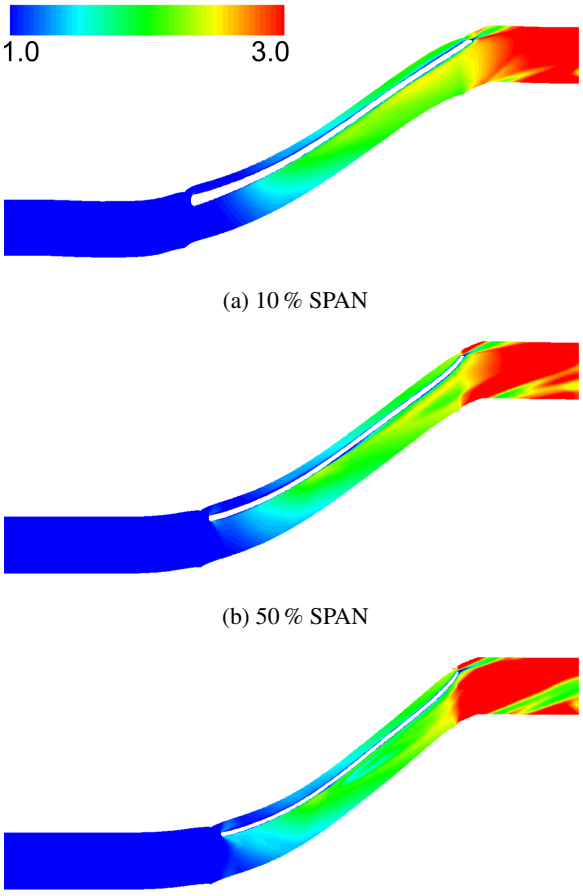

(a) 10 % SPAN

(b) 50 % SPAN

(c) 75 % SPAN

FIGURE 14: RELATIVE MACH NUMBER OF OPTIMIZED GEOMETRY WITH SUBSONIC INFLOW

the total pressure ratio significantly to 3.35, while the total temperature ratio nearly maintains at 1.236. The reduction of shaft power can be explained by the missing shock impingement patterns on the pressure side. In conclusion, the optimized geometry is able to handle supersonic and subsonic inflow, which allows to use the turbine in numerous application without the need of a (Laval) nozzle to generate supersonic inflow.

In terms of the highly fluctuating inlet condition of an RDC, the turbine demonstrates good starting behavior over a wide range of operating conditions. Alternatively, it is possible to decelerate the flow of a RDC below sonic speed and to use the designed turbine with higher turbine efficiency.

Off-design analysis

Firstly, only the total inlet pressure was changed to analyze the aerodynamic behavior under changing boundary conditions. The total temperature and static values of temperature and pres-

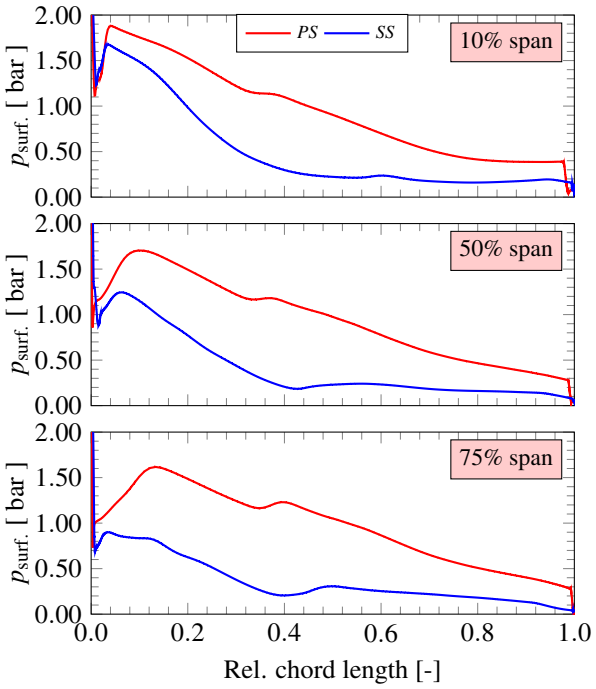

FIGURE 15: SURFACE PRESSURE PROFILES 10 %, 50 %, AND 75 % SPAN WITH SUBSONIC INFLOW

Supersonic Inflow				
$\dot{m}$ [$\mathrm{kg\,s^{-1}}$]	1.111	1.481*	1.852	2.222
$\dot{m}_{red.}$ [$\mathrm{kg\,s^{-1}\,bar^{-1}\,K^{0.5}}$]	16.14	16.14*	16.14	16.14
$\dot{W}$ [kW]	619	832*	1044	1253
η_{tt} [%]	64.6	65.4*	65.7	65.4
π_{tt} [-]	4.905	4.859*	4.849	4.891
$\frac{T_{t,in}}{T_{t,out}}$	1.241	1.243*	1.245	1.242
$p_{t,in}$ [bar]	3.290	4.386*	5.483	6.579
Subsonic Inflow				
$\dot{m}$ [$\mathrm{kg\,s^{-1}}$]	1.111	1.481	1.852	2.222
$\dot{m}_{red.}$ [$\mathrm{kg\,s^{-1}\,bar^{-1}\,K^{0.5}}$]	25.47	25.51	25.54	25.57
$\dot{W}$ [kW]	602	807	1012	1218
η_{tt} [%]	77.8	79.1	80.0	80.4
π_{tt} [-]	3.406	3.352	3.314	3.307
$\frac{T_{t,in}}{T_{t,out}}$	1.234	1.236	1.236	1.237
$p_{t,in}$ [bar]	2.081	2.770	3.457	4.146

TABLE 4: INLET TOTAL PRESSURE VARIATION FOR SUPERSONIC AND SUBSONIC INFLOW WITH AN INLET MACH NUMBER OF 2 AT 937 $\mathrm{rpm/K^{0.5}}$; * CORRESPONDS TO THE DESIGN CONDITION OF THE OPTIMIZATION

sure were kept constant. Table 1 lists all relevant non-dimensional parameters for the evaluated operating points. Variations of the total inlet pressure do not affect the running point for supersonic or subsonic inlet conditions. Total pressure ratio as well as the reduced mass flow maintain constant. Following, also the efficiency does not vary significantly over a wide range of total pressure variations. This might make the performance of supersonic and transonic radial turbines resistant against total pressure pulses. At the same time the power output increases linearly when the total pressure is rising, since more mass flow is expanded.

Secondly, for analyzing different running points in terms of reduced numbers, total pressure and total temperature were maintained constant with the values mentioned in Tab. 1 and inlet Mach number plus rotational speed were varied independently. For the subsonic inflow case the inflow Mach number is a result of the throat geometry and rotational speed (as soon as the critical pressure ratio is surpassed) and thus, cannot be influenced by the boundary conditions. Hence, only variations of the rotational speed were simulated for this type of inflow.

Figure 16 depicts the efficiency and the power output of the simulated cases in stationary off-design conditions. Note that when the inlet Mach number was reduced below 1.8, the turbine did not start anymore. Thus, a zone spans from 21 to 25 $\mathrm{kg\,s^{-1}\,bar^{-1}\,K^{0.5}}$, where the turbine cannot operate as it can be seen in Fig. 16. When the Mach number is increased up to Mach numbers around 2.5 the flow starts to separate at the shroud and the passage chokes. It can be seen that efficiency and power output are increasing, when the inlet Mach number is reduced and the rotational speed increased. Reduced Mach numbers result in a weaker leading edge shock so that higher efficiencies can be achieved. At the same time, more mass flow is ingested for lower Mach numbers which increases the power output. The highest efficiency in supersonic inlet condition of 71.8% was achieved with an inlet Mach number of 1.8. However, this running point is very close to the starting limit. By cutting back the leading edge even further, this effect could be exploited even more.

The variation of speed with subsonic inflow shows a maximum at design speed. An increase of the speed causes growing incidence losses, so that the initial trend of growing efficiencies is inverted. The efficiency could not be improved by changing the operating condition.

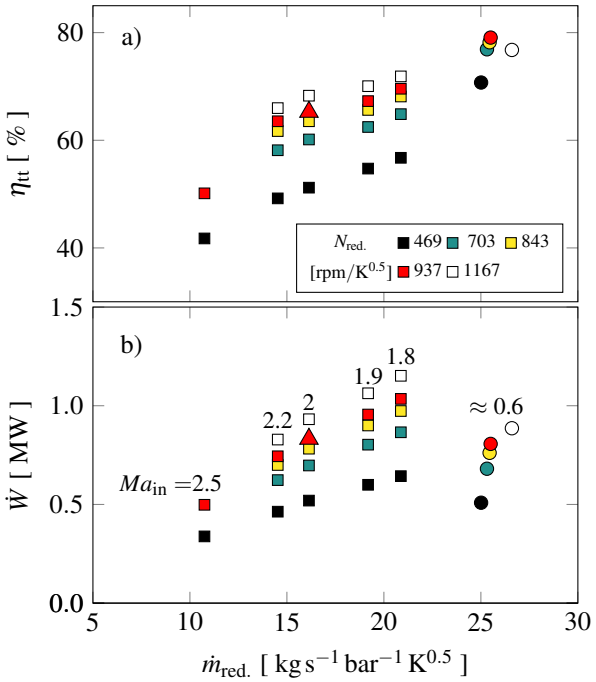

FIGURE 16: EFFICIENCY MAP (a)) AND POWER MAP (b)) FOR DIFFERENT ISO-SPEEDLINES AND VARYING INLET MACH NUMBER; SQUARES REPRESENT SUPERSONIC INLET CONDITIONS; CIRCLES REPRESENT SUBSONIC BOUNDARY CONDITIONS; THE TRIANGLE CORRESPONDS TO THE DESIGN CONDITION OF THE OPTIMIZATION

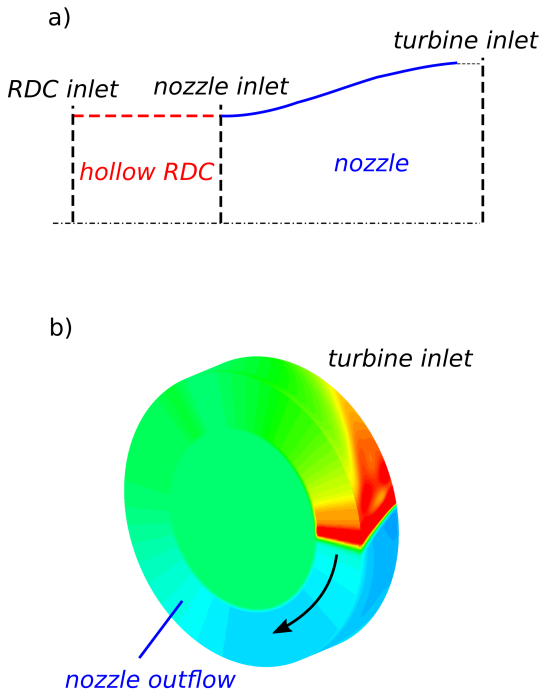

FIGURE 17: ROTATING DETONATION COMBUSTOR SETUP: a) CENTERBODYLESS RDC SETUP, b) TURBINE INLET CONDITION

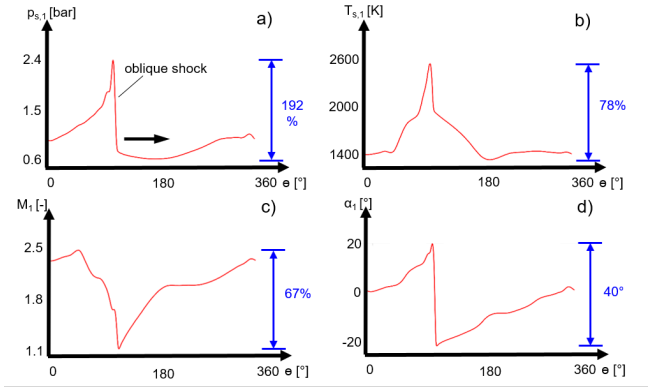

FIGURE 18: ROTATING DETONATION COMBUSTOR DATA WITH a) STATIC PRESSURE, b) STATIC TEMPERATURE, c) ABSOLUTE MACH NUMBER, d) ABSOLUTE FLOW ANGLE

Unsteady RDC inflow

Inlet condition For this study, the designed turbine was assessed with the flow of a hollow RDC such as described by Stoddard et al. [31] and Anand et al. [32, 33]. In the chosen setup the exhaust flow of the RDC was further accelerated by means of a divergent nozzle to finally achieve a mass flow averaged Mach number of 2. The resulting flow field 20 mm upstream of the turbine wheel is shown in Fig. 17 b). Due to the short circumference only one moving oblique shock was modeled to rotate in positive θ-direction.

As shown, the flow field is characterized by high unsteadiness. Static pressure fluctuations of 192 %, total temperature fluctuations of 78 %, and Mach number fluctuations of 67 % appear in the inlet flow as it is presented in Fig. 18. The core flow was modeled with steady boundary conditions at Mach 2. To avoid a breakdown of the inlet flow the static pressure had to be set to the mean value of the surrounding RDC pressure and the velocity to 85 % of the average axial velocity of the RDC flow. The static temperature was set to 1000 K to achieve the same Mach number as the surrounding flow.

Unsteady numerical settings Finally, the optimized geometry (under steady flow conditions) was assessed with the aforementioned highly transient flow of a hollow RDC. URANS simulations with a time step of 5.7×10^{-7} s and 25 internal iteration steps were performed by means of the CFD solver CFD++.

Thus, one entire rotation of the oblique shock was resolved by 300 time steps. During this period the rotor rotates by 45.6 deg. The entire rotor with 10 blades was modeled with 37M cells.

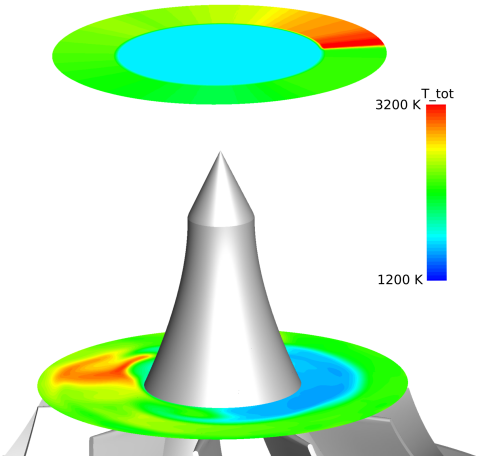

FIGURE 19: RDC FLOW FIELD DISTORTION FROM DOMAIN INLET TO PASSAGE INLET

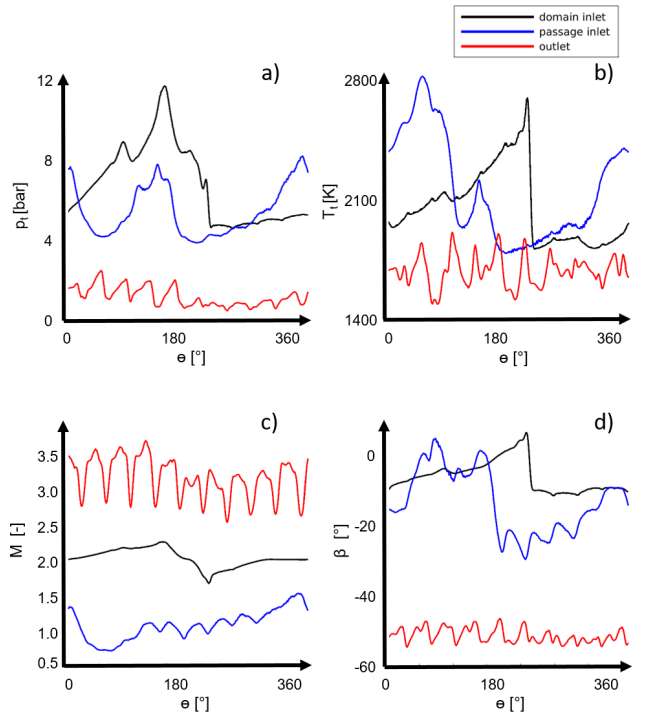

FIGURE 20: a) TOTAL PRESSURE, b) TOTAL TEMPERATURE, c) ABSOLUTE MACH NUMBER PULSES, d) RELATIVE FLOW ANGLE AT DOMAIN INLET, PASSAGE INLET, AND 30 mm BEHIND THE TRAILING EDGE AT ONE TIME STEP (RADIALLY MASSFLOW AVERAGED VALUES IN THE INLET; AXIALLY MASSFLOW AVERAGED VALUES IN THE OUTLET)

Unsteady flow results As plotted in Fig. 19, the rotating oblique shock mixes with the core flow before reaching the passage of the rotor. Following, the peak in total temperature is spread from 10 % to 90 % span of the flow passage. Over a range of 170 deg high total temperatures of the RDC flow reach the hub. On opposing side the radial thickness of the RDC flow is reduced. The radial and circumferential mixing leads to an increase of radially averaged total temperature at the passage inlet (visible in Fig. 20). Due to the mixing with the core flow and the inflow shock pattern, the radially mass flow averaged total pressure peak intensity appears reduced and the peak is divided into two total pressure peaks. Inflow shocks and the overall inflow geometry lead to a considerable deceleration of the flow up to transonic Mach numbers. However, due to the capability to start with subsonic inflow the turbine remains started in all turbine passages so that outlet flow Mach numbers are oscillating around 3. Thus, the reduced Mach number allows to have less leading edge shock losses. In general, total pressure, total temperature relative flow angle variations are damped noticeably through the rotor passage. Fluctuations in the outlet Mach number appear due to the mixing of the wake effect. The relative flow angle is reduced up to 20 deg before entering the rotor passage. This reduction occurs due to the increase of radius in the inlet section, while the inlet flow has a mass flow averaged absolute flow angle α of zero (Fig. 18). Highest values of the inlet flow angle are inherent to the oblique shock. This way the flow that follows the oblique shock front needs to be turned the most. The relative flow angle at the outlet is relatively constant and reaches values up to -55 deg.

Figure 21 and Fig. 22 show the relative Mach number and relative total pressure at mid span over one entire cycle. It can be seen how the oblique shock rotates in the same direction as the rotor. Just before the LE, the flow behind the oblique shock becomes subsonic, allowing lower leading edge shock losses when then pressure peak enters the passage. Furthermore, over the entire circumference upstream the LE, a complex system of weak shocks can be identified. This shock pattern comes from the inlet cone at the hub and the shock at the shock reflection at the shroud (Fig. 10). Upstream of the LE a complex Mach number distribution is visible. At the LE weak leading edge shocks appear due to the locally low supersonic flow. Before the oblique shock hits the blade compression waves cause relative Mach number below one at the pressure side of the inducer. At mid-chord the flow of the oblique shock creates spots of extreme acceleration on the SS, which leaves the blade passage flow to expand and to

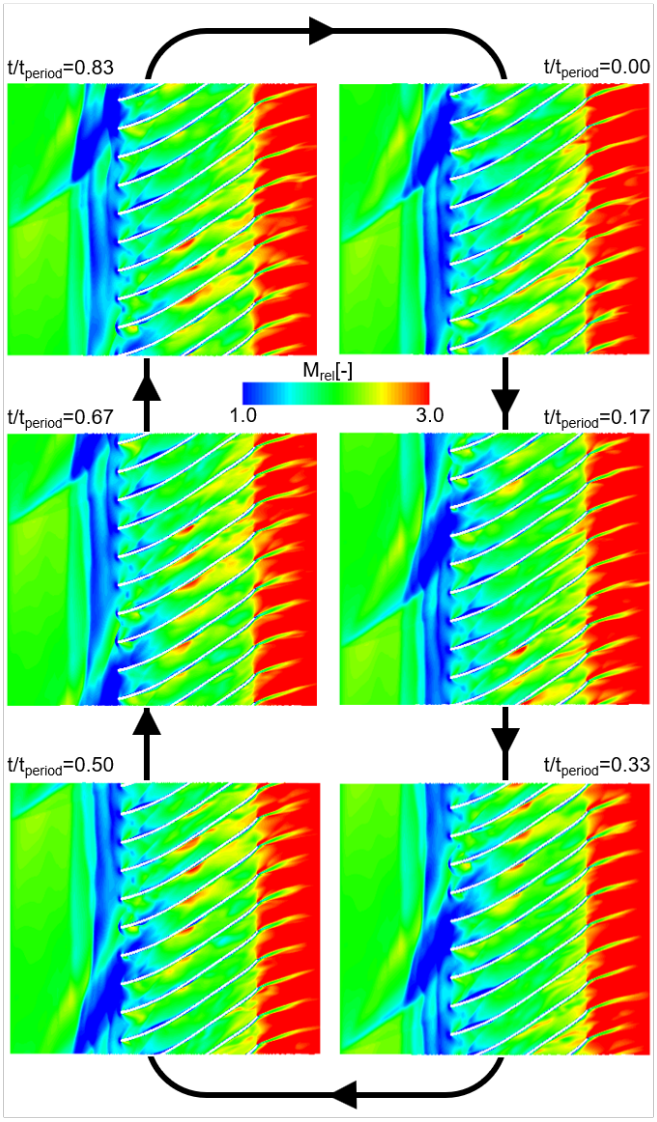

FIGURE 21: RELATIVE MACH NUMBER SNAP SHOTS AT 50 % SPAN FOR ONE PERIOD

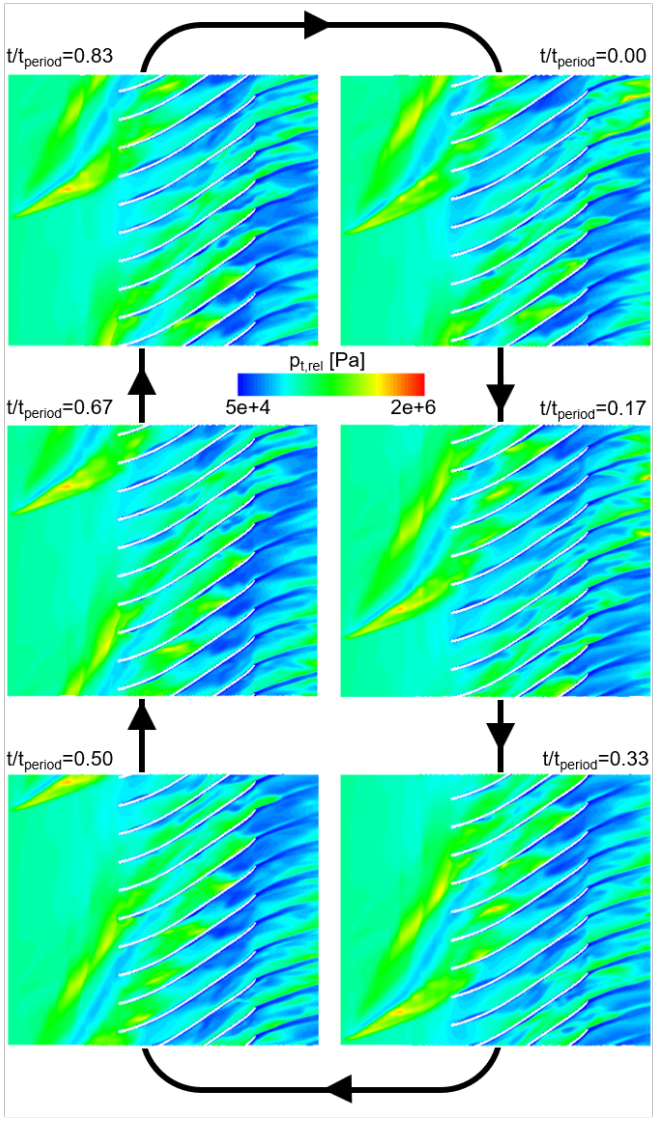

FIGURE 22: RELATIVE TOTAL PRESSURE SNAP SHOTS AT 50 % SPAN FOR ONE PERIOD

accelerate up to absolute Mach numbers of around 3.5.

Figure 22 plots the system of weak shocks at the inlet which barely create total pressure loss. A similar trend is observed for the LE shock. Figure 23 represents the surface static pressure curves for the same time instances as represented in Fig. 21 and Fig. 22. Due to the rotating shock static pressure maxima on the PS are significantly higher than with steady flow. The time instance with the lowest maximum on the PS is still higher than in steady conditions (Fig. 12). It is worth highlighting that the fluctuations of static wall pressure on the SS are of much lower magnitude. While static surface pressure fluctuations become less on the PS towards lower spans, fluctuations on the SS are slightly increasing. Hence, highest blade loading and highest amplitudes of blade loading fluctuations can be expected in the inducer at higher spans. Downstream that location, the blade loading decreases continuously.

An over one entire cycle time averaged power of 1.41 MW was obtained with the transient boundary condition of the hollow RDC. This is an increase of 70 % (while the mass flow is increased by 80 %) compared to the steady supersonic inflow in Tab. 1 with the same average inlet Mach number. The reason for the non-proportional increase of power to mass flow might be the lower core total temperature in the core of the hollow RDC setup and small efficiency penalties in transient conditions.

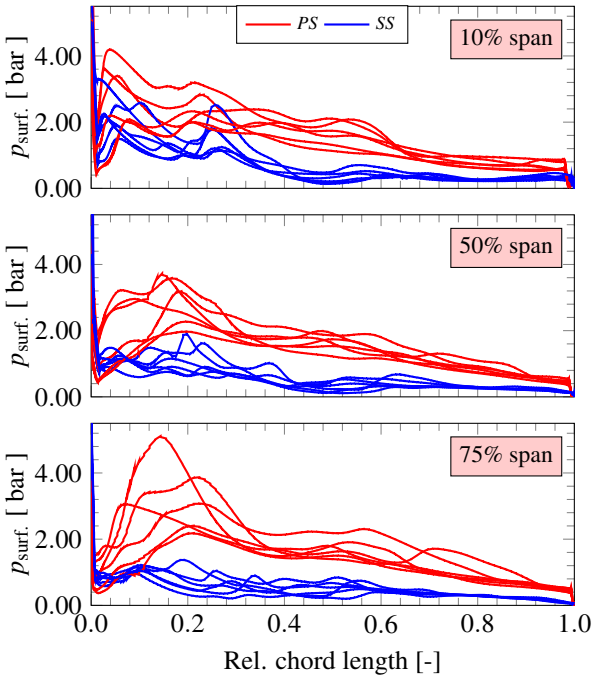

FIGURE 23: TRANSIENT SURFACE PRESSURE PROFILES 10 %, 50 %, AND 75 % SPAN WITH THE INFLOW OF A HOLLOW RDC

CONCLUSIONS

A Mach 2 supersonic axial inlet and radial outflow turbine was designed to produce a baseline configuration. The resulting turbine geometry was subsequently optimized using a genetic multi-objective optimization procedure with twelve design parameters to define the blade surface, hub, and shroud. The leading edge was cut back to the same passage inlet area ratio as in the baseline to ensure good self-starting behavior. The optimization resulted in 768 converged individuals with started supersonic inflow. The optimized turbine geometry displays an extended inlet bulb, increasing the passage height causing flow acceleration, and high blade turning, the expansion of the passage cross section is mainly caused by the growing passage height. Compared to the baseline design, the performance was enhanced by 728kW of shaft power, delivering a total-to-total efficiency of 65.4%. The specific shape of the optimized axial inflow radial outflow turbine enables ingestion of subsonic flow and converting it to supersonic outflow. This reduces LE shock losses significantly, so that total-to-total efficiencies of 79.1% were achieved. The analysis at off-design conditions revealed unstarted turbine passages for Mach numbers below 1.8, close to this value the turbine experiences its peak efficiency. The optimized turbine was modeled with highly transient supersonic inflow of a hollow rotating detonation combustor. The power extraction with this inflow enhances the shaft power by 70% compared to the steady supersonic inflow.

A future experimental demonstration of the present turbine will require the design of a cooling system to ensure long creep life. Furthermore, stress and dynamic analysis should be performed, as well as evaluations of the blade lifetime. During this process it is likely the design of the turbine may need to be revised to ensure that the lifetime of the blade remains within the required number of cycles.

ACKNOWLEDGMENTS

Lukas Inhestern was partially supported by FEDER and the Spanish Ministry of Economy and Competitiveness through grant number TRA2016-79185-R. His research stay as visiting scholar at Pudue University was additionally funded by Politécnica de Valencia. The authors would also like to acknowledge the US Department of Energy for the part-time faculty appointment of Prof. Paniagua to the Faculty Research Participation Program at the National Energy Technology Laboratory. Special thanks to Zhe Liu for his assistance in the validation of the CFD solver.

References

[1] Andreoli, V., Braun, J., Paniagua, G., Maesschalck, C. D., Bloxham, M., Cummings, W., and Langford, L. "Aerothermal optimization of fully cooled turbine blade tips". *Journal of Turbomachinery, Proceedings of the ASME Turbo Expo, June 2018, GT2018-75099, Oslo*.

[2] Sousa, J., Braun, J., and Paniagua, G., 2017. "Development of a fast evaluation tool for rotating detonation combustors". *Applied Mathematical Modelling. 52: 42-52*.

[3] Heiser, W. H., and Pratt, D. T., 2002. "Thermodynamic cycle analysis of pulse detonation engines". *Journal of Propulsion and Power, 18(1), pp. 68-76*.

[4] Ornano, F., Braun, J., Saracoglu, B. H., and Paniagua, G., 2017. "Multi-stage nozzle-shape optimization for pulsed hydrogen-air detonation combustor". *Advances in Mechanical Engineering, 9(2): 1-9*.

[5] Braun, J., Saracoglu, B. H., and Paniagua, G., 2016. "Unsteady performance of rotating detonation engines with different exhaust nozzles". *Journal of Propulsion and Power, 33(1): 121-130*.

[6] Roy, A., Ferguson, D. H., Sidwell, T., OMeara, B., Strakey, P., Bedick, C., and Sisler, A., 2017. "Experimental study of rotating detonation combustor performance under preheat and back pressure operation". *55th AIAA Aerospace Science Meeting, January 9-13, Grapevine, Texas. AIAA 2017-1065*.

[7] Le Naour, B., Falempin, F. H., and Coulon, K., 2017. "Mbda r and t effort regarding continuous detonation wave engine for propulsionstatus in 2016". *21st AIAA Interna-*

tional Space Planes and Hypersonics Technologies Conference, March 6-9, Xiamen, China. AIAA 2017-2325.

[8] Nakagami, S., Matsuoka, K., Kasahara, J., Kumazawa, Y., Fujii, J., Matsuo, A., and Funaki, I., 2017. "Experimental visualization of the structure of rotating detonation waves in a disk-shaped combustor". *Journal of Propulsion and Power, Vol. 33, No. 1, pp. 80-88.*

[9] Zhou, R., and Wang, J.-P., 2013. "Numerical investigation of shock wave reflections near the head ends of rotating detonation engines".

[10] Frolov, S., Dubrovskii, A., and Ivanov, V., 2013. "Three-dimensional numerical simulation of operation process in rotating detonation engine". *Proceedings of the Progress in Propulsion Physcis, 4: 467-488*.

[11] Fievisohn, R. T., and Yu, K. H., 2016. "Steady-state analysis of rotating detonation engine flowfields with the method of characteristics". *Journal of Propulsion and Power, 33(1): 89-99*.

[12] Paniagua, G., Lorio, M., Vinha, N., and Sousa, J., 2014. "Design and analysis of pioneering high supersonic axial turbines". *International Journal of Mechanical Sciences, 89: 65-77*.

[13] Liu, Z., Braun, J., and Paniagua, G., 2017. "Performance of axial turbines exposed to large fluctuations". *Proceedings of the 53rd AIAA/SAE/ASEE Joint Propulsion Conference, July 10-12, Atlanta, GA. AIAA 2017-4817*.

[14] Paniagua, G., Lorio, M., Vinha, N., and Sousa, J., 2014. "Design and analysis of pioneering high supersonic axial turbines". *International Journal of Mechanical Sciences, 89: 65-77*.

[15] Kantrowitz, A., and Donaldson, C., 1945. "Preliminary investigation of supersonic diffusers". *National Advisory Committee for Aeronautics, NACA-WR-L-713*.

[16] Sousa, J., Paniagua, G., and Morata, E. C., 2017. "Thermodynamic analysis of a gas turbine engine with a rotating detonation combustor". *Applied Energy, 195: 247-256*.

[17] Huff, R., Polanka, M. D., McClearn, M. J., Schauer, F., Fotia, M. L., and Hoke, J. "A disk rotating detonation engine driven auxiliary power unit". *2018 Joint Propulsion Conference, AIAA Propulsion and Energy Forum, (AIAA 2018-4879)*.

[18] Higashi, J., Nakagami, S., Matsuoka, K., Kasahara, J., Matsuo, A., Funaki, I., and Moriai, H. "Experimental study of the disk-shaped rotating detonation turbine engine". *55th AIAA Aerospace Sciences Meeting, AIAA SciTech Forum, (AIAA 2017-1286)*.

[19] Akbari, P., and Polanka, M. D. "Performance of an ultra-compact disk-shaped reheat gas turbine for power generation". *2018 Joint Propulsion Conference, AIAA Propulsion and Energy Forum, (AIAA 2018-4878)*.

[20] McKain, T. F., and Holbrook, G. J., 1997. "Coordinates for a high performance 4: 1 pressure ratio centrifugal compressor".

[21] Chakravarthy, S., Peroomian, O., Goldberg, U., and Palaniswamy, S., 1998. "The cfd++ computational fluid dynamic software suite". *AIAA and SAE, World Aviation Conference, Anaheim, CA*.

[22] Liu, Z., Braun, J., and Paniagua, G., 2019. "Characterization of a supersonic turbine downstream of a rotating detonation combustor". *Journal of Engineering for Gas Turbines and Power, Vol. 141, No.3, p. 031501*.

[23] Paniagua, G., Yasa, T., De La Loma, A., Castillon, L., and Coton, T. "Unsteady strong shock interactions in a transonic turbine: Experimental and numerical analysis". *Journal of Propulsion and Power,* ***24***(4).

[24] Verstraete, T., 2010. "Cado: a computer aided design and optimization tool forturbomachinery applications". *2nd International Conference on Engineering Optimization*.

[25] Verstraete, T. T., Alsalihi, Z. Z., and Van den Braembussche, R. A., 2010. "Multidisciplinary optimization of a radial compressor for microgas turbine applications". *Journal of Turbomachinery, Vol. 132, No. 3, p. 031004*.

[26] De Maesschalck, C., S., L., and G., P., 2013. "Blade tip shape optimization for enhanced turbine aerothermal performance". *ASME Turbo Expo: Power for Land, Sea, and Air, Volume 3C: Heat Transfer ():V03CT14A011*.

[27] Braun, J., Sousa, J., and Pekardan, C., 2017. "Aerodynamic design and analysis of the hyperloop". *AIAA Journal, Vol. 55, No. 12 (2017), pp. 4053-4060.*

[28] Sousa, J., Paniagua, G., and Collado-Morata, 2010. "Analysis of the aerodynamic lossess in a supersonic turbine". *Proceedings of the ASME 2017 Power Conference Joint with ICOPE-17, June 26-30, Charlotte, NC. POWER-ICOPE2017-3624*.

[29] Serrano, J. R., García-Cuevas, L. M., Inhestern, L. B., Guilain, S., and Tartoussi, H., 2018. "Analysis of unsteady energy fluxes in a turbocharger by using a holistic model extrapolating standard lookup tables in full engine operating map". In ASME Turbo Expo 2018: Turbomachinery Technical Conference and Exposition, American Society of Mechanical Engineers, pp. V008T26A015–V008T26A015.

[30] Liu, Z., Braun, J., and Paniagua, G., 2018. "3d optimization of a subsonic axial turbine designed for high inlet mach number". *Proceedings of the 54th AIAA/SAE/ASEE Joint Propulsion Conference, AIAA Propulsion and Energy Forum*.

[31] Stoddard, W., George, A. C. S., Driscoll, R. B., Anand, V., and Gutmark, E. J. "Experimental validation of expanded centerbodiless rde design". *54th AIAA Aerospace Sciences Meeting, AIAA SciTech Forum, (AIAA 2016-0128)*.

[32] Anand, V., and Gutmark, E., 2018. "Rotating detonation combustor research at the university of cincinnati". *Flow Turbulence and Combustion*, 05.

[33] Anand, V., St. George, A., and Gutmark, E., 2016. “Hollow rotating detonation combustor”. *Conference: AIAA Scitech 2016, At San Diego*.